RSC Advances

ROYAL SOCIETY OF CHEMISTRY

www.rsc.org/advances

PEDOT:PSS assisted preparation of graphene/nickel cobalt oxide hybrid counter electrode and served in efficient dye-sensitized solar cells

Gentian Yue[†, *], Guang Yang[†], Fumin Li[†], Jihuai Wu[‡]

[†] *Key Laboratory of Photovoltaic Materials of Henan and School of Physics & Electronics, Henan University, Kaifeng 475004, China*;

[‡] *Institute of Material Physical Chemistry, Huaqiao University, Xiamen 361021, China*

Keywords: Grephene; nickel cobalt oxide; poly (3, 4-ethylenedioxythiophene):poly (styrenesulfonate); counter electrode; dye-sensitized solar cells

∗ Corresponding author. +86 371 23881602, E-mail address: yuegentian@henu.edu.cn (G. Yue).

Abstract: The graphene/nickel cobalt oxide ($Gr/NiCo_2O_4$) hybrids with nanostructure was prepared by the use of an in situ hydrothermal route, and applied as a counter electrode (CE) with poly (3, 4-ethylenedioxythiophene) : poly (styrenesulfonate) assisted preparation (here abbreviated as P-A) in dye-sensitized solar cells (DSSCs) for the first time. The surface morphology of bilayer TiO_2 photoanode was confirmed by using the scanning electron microscopes. The superior structural characteristic for the photoanode was advantageous to fast mass transport for the electrolyte, increased the contact area between electrolyte and active materials, and enabled the (P-A) $Gr/NiCo_2O_4$ CE to speed up the reduction of triiodide to iodide. Also, the CE with superiority nanostructure was evaluated by electrochemical characterizations, which indicated that the (P-A) $Gr/NiCo_2O_4$ CE possessed excellent electrocatalytic activity in iodide/triiodide electrolyte and lower charge transfer resistance of 3.04±0.02 $\Omega \cdot cm^2$ compared to the Pt electrode (3.63±0.02 $\Omega \cdot cm^2$). Under optimum conditions, the DSSC based on the (P-A) $Gr/NiCo_2O_4$ CE achieved a remarkable power conversion efficiency of 8.10%, higher about 8.7% than that of the DSSC Pt-based (7.45%). The (P-A) $Gr/NiCo_2O_4$ CE can be considered as a promising alternative CE for Pt-free DSSCs.

1. Introduction

Dye-sensitized solar cells (DSSCs), electrochemical devices converting solar energy to electricity characterized by high conversion efficiency, are honored as promising solution to energy depletion, environmental pollution and ecological destruction for their low-cost, environment-friendly and good durability.[1-3] Typically, the device consists of dye adsorbed TiO_2 nanoparticles, filled with electrolyte containing iodine/triiodine (I^-/I_3^-) redox couples, and counter electrode (CE) with excellent catalytic ability. Conventionally, CE, as the most important component in a DSSC, collects the electrons from the external circuit and catalyzes reduction of I_3^- to I^- between the CE and electrolyte interface.[4,5]

The graphene and its hybrids have been believed as an efficient approach in enhancing the photoelectric and electrochemical performance of DSSCs.[6-11] The large surface area, unique features of the strong mechanical strength, high electrical and thermal conductivity associated with graphene usually translate into high efficiency for the photoelectric chemical devices,[12,13] so it was highly desirable for applications in DSSCs.[14] Moreover, as one of transition metal oxides, $NiCo_2O_4$ with much remarkable electrical conductivity has attracted considerable attentions as a low over-potential catalyst for oxygen reduction reactions and a high-performance electrode material in Li-ion battery, supercapacitor and fuel cell for its low-cost, environmental friendliness.[15-21] It is therefore expected to offer richer redox reactions, including contributions from both nickel and cobalt ions, than those of the monometallic nickel oxide or cobalt oxide. Simultaneously, the electrochemical performance is also affected by the morphology of the $NiCo_2O_4$ catalyst, e.g., 1D nanomaterials have demonstrated better performance for $Li–O_2$ batteries than micro-particles.[22,23]

Therefore, taking into account of all these factors, in search for more robust Pt-free CEs, here we reported the graphene/nickel cobalt oxide ($Gr/NiCo_2O_4$) hybrids with nanostructure through an in situ hydrothermal route and prepared an efficient $Gr/NiCo_2O_4$ CE with poly (3, 4-ethylenedioxythiophene):poly (styrenesulfonate) (PEDOT:PSS) assisted (here abbreviated as P-A) by means of slurry-coating technique. This type of electrode was generally anticipated with many advantages, such as good electrical conductivity, easy electrolyte penetration, and high electrochemical activity. The electrocatalytic ability and photoelectric property for the DSSC (P-A) ($Gr/NiCo_2O_4$)-based was systematically investigated. The DSSC assembled with the (P-A) ($Gr/NiCo_2O_4$) CE exhibited a considerably improved performance in photo-electric conversion efficiency of 8.10% under irradiation of

100 $mW \cdot cm^{-2}$ (AM 1.5 G).

2. Experimental

2.1 Materials

The nickel (II) nitrate hexahydrate ($Ni(NO_3)_2 \cdot 6H_2O$, 98%), cobalt (II) nitrate hexahydrate ($Co(NO_3)_2 \cdot 6H_2O$, 98.5%), poly (styrenesulfonate) (PSS), 3, 4-ethylenedioxythiophene (EDOT), N-methyl-2-pyrrolidinone (NMP), polyvinyl-difluoride (PVDF), potassium persulfate ($K_2S_2O_8$) and titanium tetrachloride ($TiCl_4$) were purchased from Shanghai Chemical Agent Ltd, China. All reagents are of analytical reagent grade. The dye N-719 cis-di(isothiocyanato)-bis-(2,2'-bipyridyl-4,4'-dicarboxylato) ruthenium(II) bis-tetrabutylammonium was obtained from Solaronix SA (Switzerland).

2.2 Preparation of (P-A) Gr/$NiCo_2O_4$ hybrid counter electrode

A typical synthesis proceeded of PEDOT:PSS outlines below. 6.95 g PSS (18 wt.%) aqueous solution was mixed with 75 ml deionized water at room temperature and treated with nitrogen bubbling for 0.5 h. Then 0.5 g EDOT and 0.0077g $Fe_2(SO_4)_3 \cdot 9H_2O$ were added to initiate the polymerization. The mixture was stirred at room temperature for 2 h, after which a further 0.1673g $K_2S_2O_8$ was added. After additional reaction 12 h, the mixture was put into a dialytic bag for 48 h to remove the excess reactants. Then the blue solution of PEDOT:PSS was obtained.

Briefly, the preparation of (P-A) Gr/$NiCo_2O_4$ counter electrode is outlined as following. Firstly, 1.0 mmol $Ni(NO_3)_2 \cdot 6H_2O$, 2.0 mmol $Co(NO_3)_2 \cdot 6H_2O$, 6.0 mmol NH_4F and 15 mmol $CO(NH_2)_2$ were dissolved in 38 ml deionized water. After ultrasonication and stirring for 30 min until a homogeneous solution was achieved. After that, 1.5 wt.% of graphene was added into the reaction solution. Further sonicated for another 30 min before transferred into Teflon-lined autoclave, and then heated in an oven at 100℃ for 10 h without intentional control of ramping or cooling rate. The Gr/$NiCo_2O_4$ hybrids with black color were collected by filter and washed with ethanol and distilled water for 5 times, followed by annealing at 200℃ for 4 h. Then, the Gr/$NiCo_2O_4$ as active material was mixed with acetylene black and PVDF in a weight ratio of 8: 1: 1. The paste of the above mentioned mixtures was prepared by the use of deionized water, ethanol, NMP and PEDOT:PSS as the solvent, respectively, and kept stirring for 12 h. Subsequently, the as-prepared paste was coated on FTO substrate (8 $\Omega \cdot cm^{-2}$, the thickness of 350 nm, Hartford Glass

Co., USA) using a doctor blade method with an area of 0.64 cm^2 to form the film with the thickness of ~6 μm. The obtained electrodes were dried at 100℃ for 12 h in a vacuum oven and marked as (W-A) Gr/$NiCo_2O_4$, (E-A) Gr/$NiCo_2O_4$, (N-A) Gr/$NiCo_2O_4$ and (P-A) Gr/$NiCo_2O_4$ CEs, respectively. For comparison, the Gr and $NiCo_2O_4$ electrodes mentioned in the manuscript were also prepared by the use of PEDOT:PSS as the solvent and signed Gr^* and $NiCo_2O_4{}^*$ CEs with a similar method. The Pt electrode was prepared by using a three-electrode system.

2.3 Fabrication of DSSC

The bilayer TiO_2 photoanode is prepared as described previously.[24,25] Firstly, a thin TiO_2 dense layer with particle size of 36 nm and thickness of 0.5 μm was prepared by spin-coating the solution (4 ml tetrabutyltitanate, 5 ml isopropanol and 1 ml acetylacetone in 25 ml n-butanol) on FTO substrate at 1500 rpm for 30 s, followed by sintering at 450℃ for 30 min in air. Secondly, the TiO_2 nanorods with diameter of about 300 nm grew on the dense layer as following. Two pieces of FTO with TiO_2 dense layer were placed into 60 ml of tetrabutyltitanate solution containing of 1 ml of tetrabutyltitanate, 30 ml of deionized water and 30 ml of hydrochloric acid (36.5%-38% by weight) at an angle against the wall of the Teflon-liner with the conducting side facing down. The hydrothermal synthesis was conducted at 160°C for 6 h in an electric oven. The dye was loaded by immersing the bilayer TiO_2 photoanode in the 0.3 mM of N719 ethanol solution for 12 h. Thus the dye-sensitized TiO_2 photoanode with thickness of 4-5 μm was obtained. The DSSC was fabricated by injecting the liquid electrolyte (0.05 M of I_2, 0.1 M of LiI, 0.6 M of tetrabutylammonium iodide and 0.5 M of 4-tertpbutylpyridine in acetonitrile) into the aperture between the dye-sensitized TiO_2 electrode and the CE. The two electrodes were clipped together and wrapped with thermoplastic hot-melt Surlyn (the schematic of DSSC shown in Fig. 1).

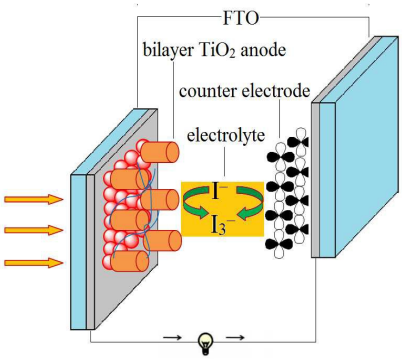

Fig. 1 Schematic of DSSC with bilayer TiO_2 photoanode and (P-A) Gr/$NiCo_2O_4$ counter electrode.

2.4. Characterization

The surface morphology of the samples was observed by using JSM-7001F field emission scanning electron microscope (SEM). Cyclic voltammetry (CV) and electrochemical impendence spectroscopy (EIS) were conducted by the use of a computer-controlled electrochemical analyzer (CHI 660D, Shanghai Chenhua Device Company, China). The electrolyte used in the DSSC test was also injected into the dummy cells for the EIS measurements. EIS was carried out under the simulating open-circuit conditions at ambient atmosphere, sealing with thermoplastic hot-melt Surlyn and leaving an exposed area of 0.64 cm^2. The frequency of applied sinusoidal AC voltage signal was varied from 0.1 Hz to 10^5 Hz and the corresponding amplitude was kept at 5 mV in all cases.

The photovoltaic test of DSSC with an exposed area of 0.4×0.7 cm^2 was carried out by measuring photocurrent-photovoltage (*J-V*) character curve under white light irradiation of 100 $mW \cdot cm^{-2}$ (AM 1.5 G) from the solar simulator (XQ-500W, Shanghai Photoelectricity Device Company, China) in ambient atmosphere. The fill factor (*FF*) and the photo-electric conversion efficiency (*PCE*) of DSSC were calculated according to the following equations:

$$\eta(\%) = \frac{V_{max} \times J_{max}}{P_{in}} \times 100\% = \frac{V_{oc} \times J_{sc} \times FF}{P_{in}} \times 100\% \quad (1)$$

$$FF = \frac{V_{max} \times J_{max}}{V_{oc} \times J_{sc}} \quad (2)$$

where J_{sc} is the short-circuit current density ($mA \cdot cm^{-2}$); V_{oc} is the open-circuit voltage (V); P_{in} is the incident light power ($mW \cdot cm^{-2}$); J_{max} ($mA \cdot cm^{-2}$) and V_{max} (V) are the current density and voltage at the point of maximum power output in the *J–V* curve, respectively.

The diffusion coefficient (D_n) of CE in electrolyte is estimated in the light of the Randles-Sevcik equation as illustrated as equation (3):

$$I_{pc} = Kn^{1.5} AC(D_n)^{0.5} v^{0.5} \quad (3)$$

where I_{pc} is the cathodic current density; K is the constant of 2.69×10^5; n means the number of electrodes contributing the charge transfer; A is the area of the CE; C and v represent the concentration of I_3^- species and the scan rate, respectively.

The exchange current density (J_0) for the Tafel curves can be estimated according to equation (4):

$$J_0 = \frac{RT}{nFR_{ct}} \quad (4)$$

where R is the gas constant; T is the temperature; F is Faraday's constant; R_{ct} is the charge transfer resistance.

3. Results and discussions

3.1 Surface morphology and composition of the TiO_2

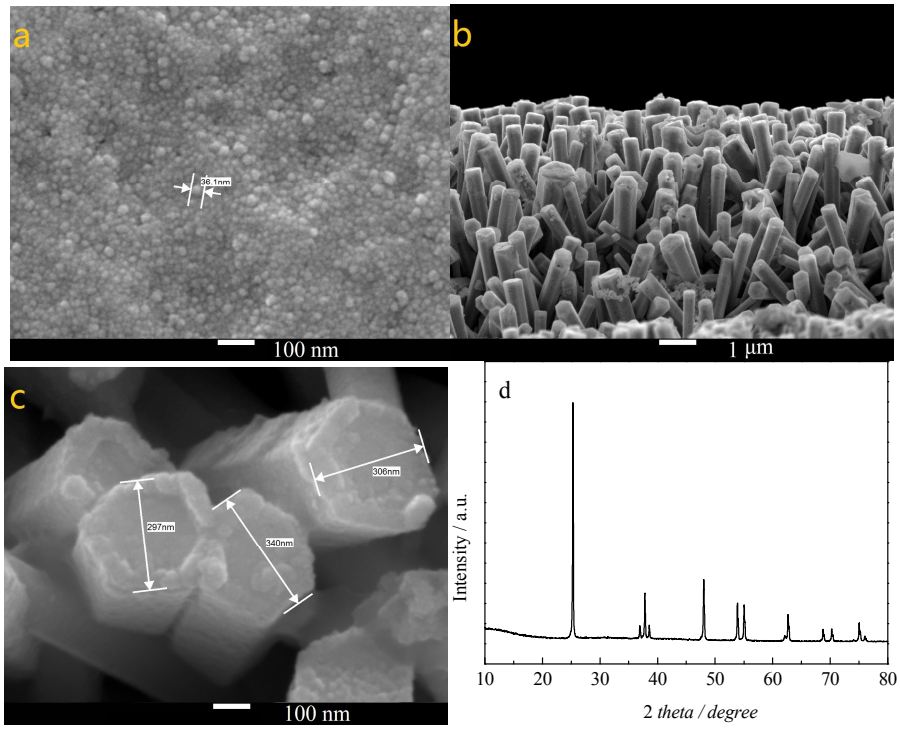

Fig. 2 The SEM images of TiO_2 dense layer (a), TiO_2 nanorods (b, c), and XRD patterns of TiO_2 nanorods (c).

Fig. 2a presents the image of TiO_2 dense layer, which shows that the TiO_2 dense layer with size of about 36 nm was prepared by using a spin-coated method to reduce the charge recombination and improve the fill factor of the DSSC. Top and side views in Fig. 2 b and c show that the top surface of the TiO_2 nanorods are nearly perpendicular to the FTO substrate and hexagonl in shape with square top facets. After 6 h of growth, the average diameter and length for the nanorods, as determined from SEM images, are about 300-340 nm and 3.5 µm, respectively. This distance favors to the photoproduction electronic transmission. Moreover, the TiO_2 nanorods grew on TiO_2 dense layer by the use of an in *situ* hydrothermal route are anatase phase as referred as the XRD patterns in Fig. 2d.

3.2. UV-vis absorption spectra

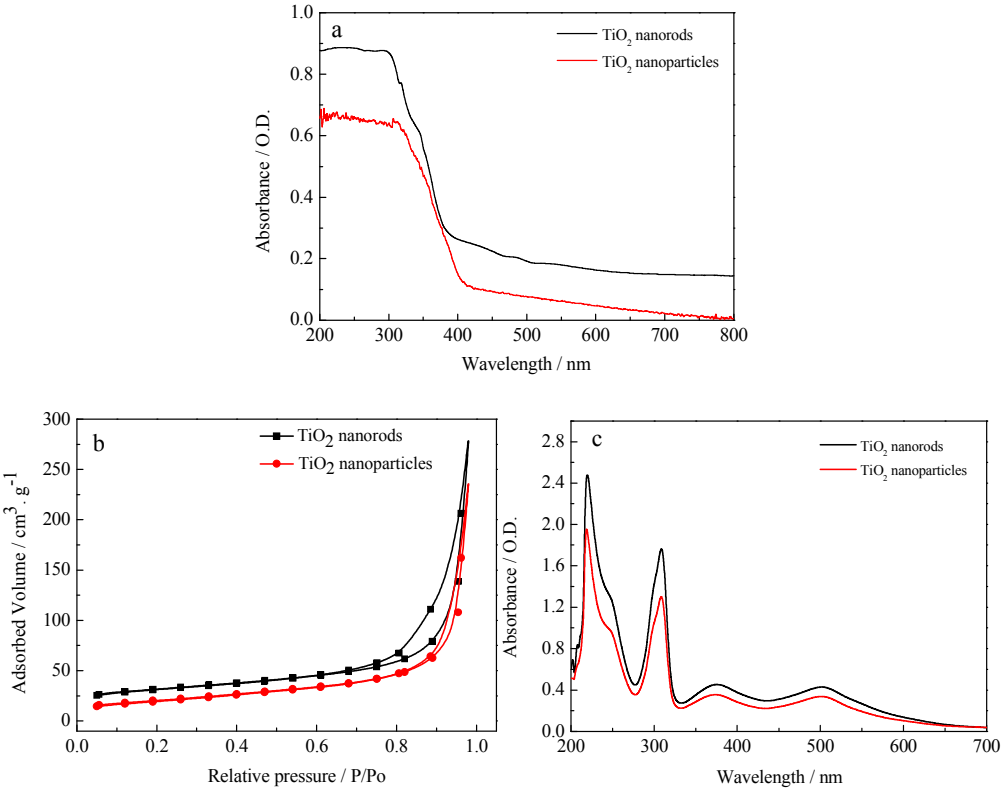

Fig. 3 UV–vis absorption spectra (a, c) and the specific surface areas (b) of TiO_2 nanorods and TiO_2 nanoparticles.

The UV-vis absorption spectra of TiO_2 with nanorods and nanoparticles structures were measured and are displayed in Fig. 3a. As expected, TiO_2 nanorods show more obviously absorption enhancement for the characteristic spectrum with its fundamental absorption of Ti–O bond in ultraviolet light range from 300 to 400 nm, mainly because of the more convenient channel for charge transport provided by TiO_2 nanorods. Fig. 3b shows the specific surface areas (Brunauer-Emmett-Teller, BET) for the different morphology of TiO_2 by nitrogen adsorption-desorption. It is clearly that the BET of the TiO_2 nanorods (105.4 $m^2 \cdot g^{-1}$) possesses much larger specific surface area than TiO_2 nanoparticles (71.3 $m^2 \cdot g^{-1}$), indicating that the TiO_2 nanorods have very uniform mesopores. Such high BET surface area could facilitate the dye-loading capacity and probably endow the TiO_2 nanorods-based DSSCs with higher current density.[26] Simultaneously, the absorption spectra of dye desorbed from the photoanodes with different structures is exhibited in Fig. 3c. It is clearly that the stronger absorption of dye for the TiO_2 photoanode with nanorods structure can be obtained than that of the nanoparticles structure, which well proved the enhanced specific surface area for the TiO_2 nanorods as shown in Fig. 3b. Furthermore, the estimated adsorbed amount of dye N719 in the photoanode with

nanoparticles structure is about 0.52×10^{-7} mol·cm^{-2}, while it can reach 0.86×10^{-7} mol·cm^{-2} for the TiO_2 nanorods photoanode.

3.3 Surface morphology and composition of the samples

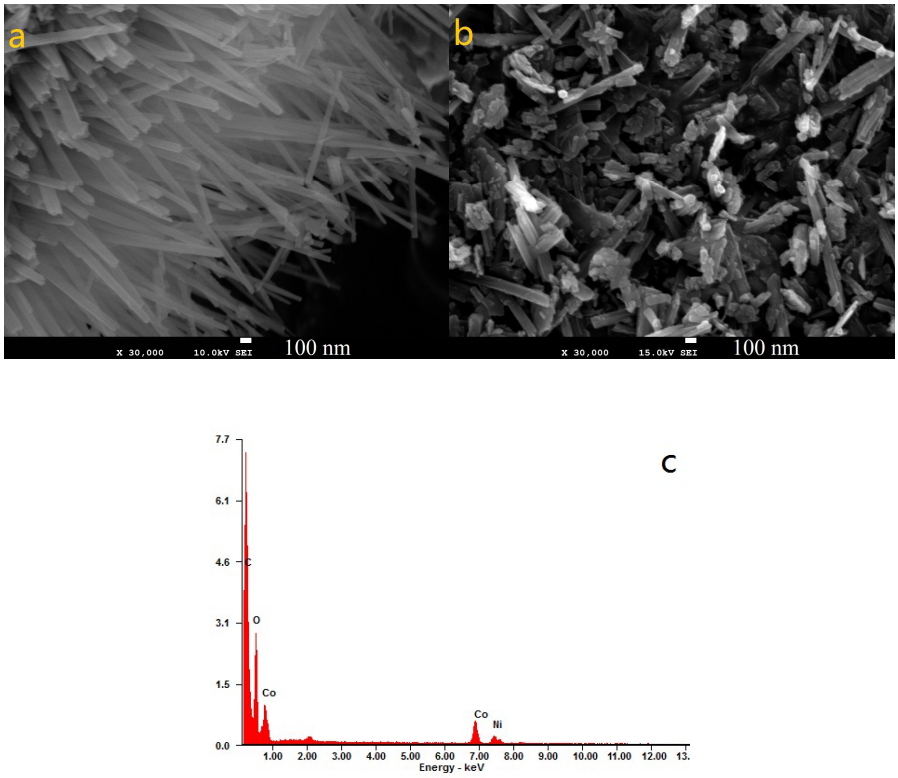

Fig. 4 The SEM images of $NiCo_2O_4$ nanorods (a), Gr/$NiCo_2O_4$ nanoparticles (b), and EDS of Gr/$NiCo_2O_4$ nanoparticles (c).

Fig. 4a and b show the SEM images of $NiCo_2O_4$ nanorods and Gr/$NiCo_2O_4$ nanoparticles. As seen as in Fig. 4a, it can be obtained that the $NiCo_2O_4$ particles exhibit a beautiful rods-like nanostructure. It is notably, when added graphene into the hydrothermal reaction solution, the morphology of the Gr/$NiCo_2O_4$ nanoparticles interestingly changed to shorter nanorods and blended uniformly with graphene flakes as shown as in Fig. 4b. The unique nanostructure guarantees full contact area and fast mass transport for the electrolyte, and enables highly enhanced catalytic activity toward the reduction of I_3^-, which logically results in considerably improved the photovoltaic performance.[27] The EDS analysis of the sample indicates the presence of C, O, Co, Ni elements and strong signals as shown as in Fig.4c, which is responsible for the formation of Gr/$NiCo_2O_4$ nanoparticles.

3.4 Electrochemical properties of counter electrode

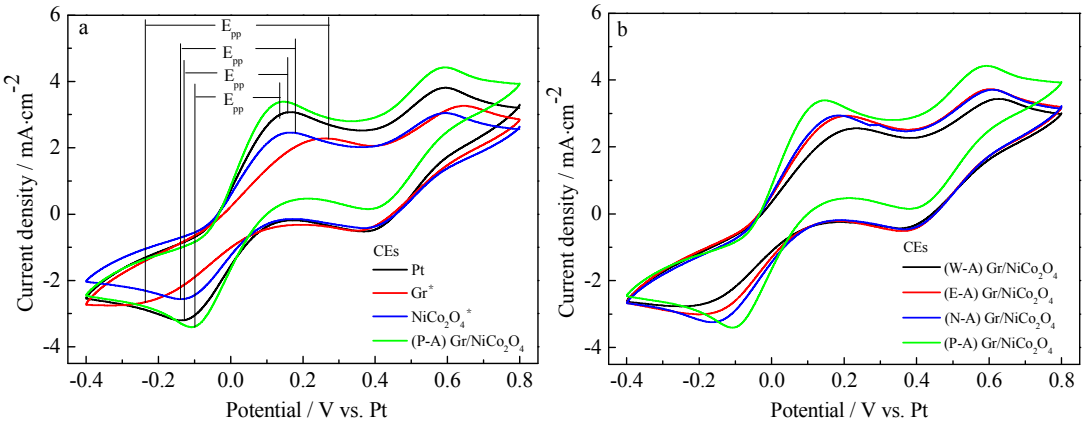

Fig. 5 CVs for the Pt, Gr*, $NiCo_2O_4$* and (P-A) Gr/$NiCo_2O_4$ CEs (a) and Gr/$NiCo_2O_4$ CE with different solvents (b) at the scan rate of 50 mV·s^{-1}.

As depicted in Fig. 5, two pairs of redox peaks are observed in the CV curves for the different CEs at a scan rate of 50 mV·s^{-1}. The left and right pairs redox peaks are associated with $I_3^- + 2e^- \leftrightarrow 3I^-$ and $3I_2 + 2e^- \leftrightarrow 2I_3^-$, respectively. The main function of CE is responsible for speed up the reduction of I_3^- to I^-, which is highly related to the left redox pair peaks. The cathodic current density (I_{pc}) and the peak to peak separation (E_{pp}) are two crucial parameters for comparing the electrocatalytic ability of various CEs.[28,29] Fig. 5a exhibits the CV curves of the Pt, Gr*, $NiCo_2O_4$* and (P-A) Gr/$NiCo_2O_4$ CEs at a scan rate of 50 mV·s^{-1}. To our knowledge, the $|I_{pc}|$ is positive correlated with the catalytic ability of electrodes; and $|E_{pp}|$ is inversely correlated with the electrocatalytic activity of the CEs. It noticed that the (P-A) Gr/$NiCo_2O_4$ CE shows the higher I_{pc} than that of the Pt, Gr* and $NiCo_2O_4$* electrodes in Fig.5a, indicating the (P-A) Gr/$NiCo_2O_4$ CE effectively acted as a catalyst in the reaction of the I^-/I_3^- electrolyte. The $|E_{pp}|$ of the above mentioned CEs increases in the orders of (P-A) Gr/$NiCo_2O_4$ CE (0.23±0.01 V) < Pt CE (0.28±0.01 V) < $NiCo_2O_4$* CE (0.32±0.01 V) < Gr*CE (0.51±0.01 V), which is immediately responsible for the lower overpotential loss in the (P-A) Gr/$NiCo_2O_4$ CE than the others since the highly conductive PEDOT:PSS was incorporated into Gr/$NiCo_2O_4$ nanoparticles. In the case of (P-A) Gr/$NiCo_2O_4$ CE, $NiCo_2O_4$ evenly coated on the graphene surface and still basically kept the morphology of the graphene network, which would effectively facilitate the electron transport and the diffusion of redox electrolyte within the CE. In addition, the synergistic effect of PEDOT:PSS also provides an efficient electron transport network and enhances conductivity of the counter electrode.

Furthermore, the reduction reaction of I^-/I_3^- redox couples occurred at different CEs belongs to the diffusion-controlled transport process, and the diffusion coefficient (D_n) is positive correlated with I_{pc} from the Randles-Sevcik equation as illustrated in Eqn. (3).[30] Though, $NiCo_2O_4$* CE has larger $|E_{pp}|$ than Gr*CE, which possesses lowest $|I_{pc}|$ among all the CEs. Thus, from which, the D_n of I_3^- for the samples follows the orders of (P-A) $Gr/NiCo_2O_4$ CE > Pt CE > Gr*CE > $NiCo_2O_4$* CE. The larger D_n for the (P-A) $Gr/NiCo_2O_4$ CE than that of the other CEs presumably originates from its well-controlled surface structure and the improvement of the conductivity of the CE.

Fig. 5b presents CVs of $Gr/NiCo_2O_4$ CEs depended on deionized water, ethanol, NMP and PEDOT:PSS as solvents, respectively. It is clearly that the influences of the solvents on the electrochemical ability are great and the relationships between the solvent vs. the $|I_{pc}|$ and $|E_{pp}|$ for the CEs are summarized in Table 1. Among them, the $|I_{pc}|$ of the above mentioned CEs increases in the orders of (W-A) $Gr/NiCo_2O_4$ CE < (E-A) $Gr/NiCo_2O_4$ CE < (N-A) $Gr/NiCo_2O_4$ < (P-A) $Gr/NiCo_2O_4$ CE, while the $|E_{pp}|$ increases in the opposite orders. The difference of electrochemical ability for the CEs prepared with various solvents mainly comes from following several aspects. PVDF, as the binder of the conductive paste, dissolves easily in NMP and ethanol, but can not dissolves in deionized water very well. However, ethanol volatilizes quickly and causes its conductive paste unstable in air. Compared to NMP and ethanol, PEDOT:PSS with excellent conductivity and catalytic ability could better dissolves PVDF and provides good network for the charge transport.[31]

Table 1 The electrochemical performance of the samples based on different CEs with various solvents.

Solvents	$\|I_{pc}\|$ ($mA \cdot cm^{-2}$)	$\|E_{pp}\|$ (V)	J_0 ($mA \cdot cm^{-2}$)	R_s ($\Omega \cdot cm^{-2}$)	R_{ct} ($\Omega \cdot cm^{-2}$)
Deionized water	2.69	0.42	1.08	8.46±0.02	4.37±0.02
Ethanol	2.97	0.39	1.16	8.13±0.02	4.02±0.02
NMP	3.24	0.34	1.20	7.69±0.02	3.84±0.02
PEDOT:PSS	3.41	0.23	1.32	6.82±0.02	3.04±0.02

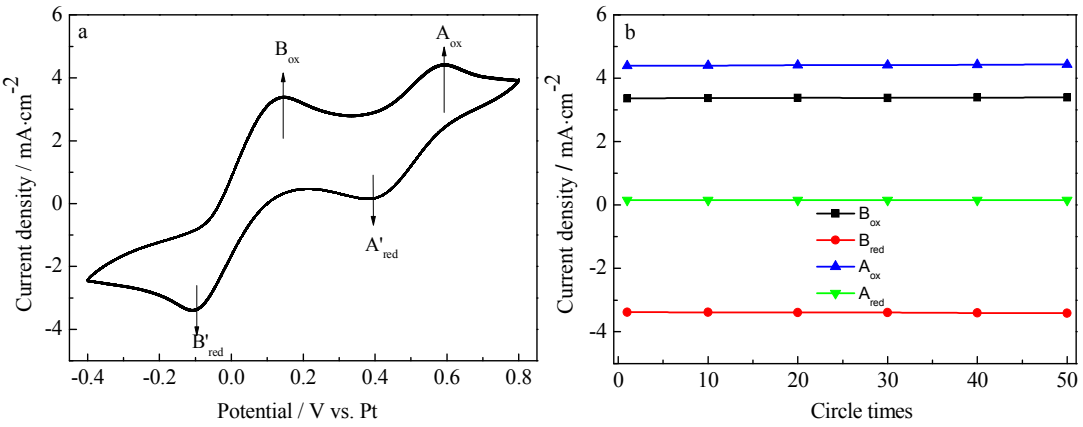

Fig. 6 40 cycles CVs (a) and the relationship between the cycles and the maximum redox peak currents for the (P-A) Gr/$NiCo_2O_4$ electrode (b).

It is very important to the performance of the DSSC of a long-term electrochemical stability of a CE. The 40-cycles consecutive cycle scan test has performed for the (P-A) Gr/$NiCo_2O_4$ CE at the scan rate of 50 mV·s^{-1} using the same electrolyte mentioned in the experimental section. After 40 CVs, the normalized cathodic and anodic peak current densities remain scarcely changed and maximum redox peak current densities show a good linear relationship as presented in Fig. 6, suggesting that the (P-A) Gr/$NiCo_2O_4$ CE is stable and not corroded in the I^-/I_3^- redox electrolyte.[32,33]

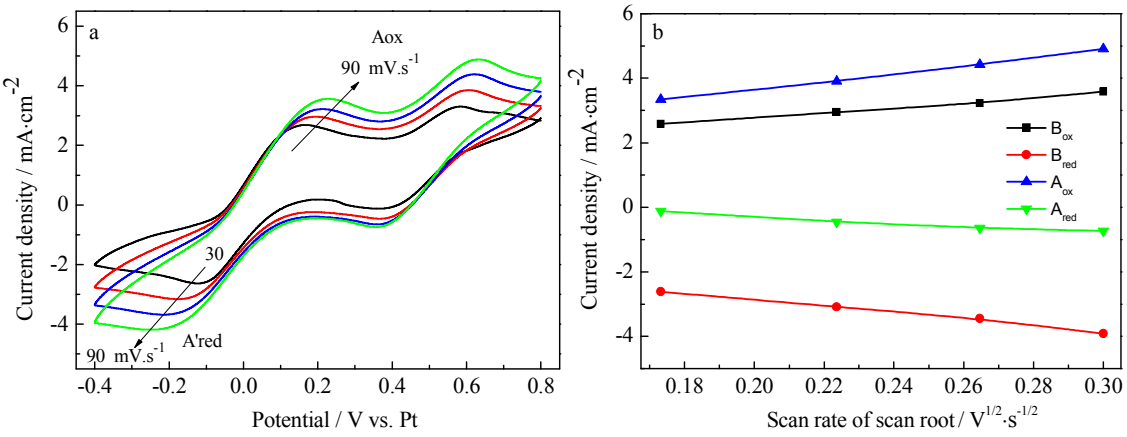

Fig. 7 CVs for the (P-A) Gr/$NiCo_2O_4$ electrode with different scan rates (from inner to outer: 30, 50, 70, 90 mV·s^{-1}) (a); and the redox peaks current versus square root of scan rates (b).

The CVs of the (P-A) Gr/$NiCo_2O_4$ electrode at various scan rates from 30 to 90 mV·s^{-1} and the relationship between the redox peaks current versus square root of scan rates as shown as in Fig. 7. It can be obviously observed

that both the oxidation and reduction peaks for the I_{pc} and potential gradually and regularly changed with the increasing scan rates; and the I_{pc} *versus* (scan rate)$^{1/2}$ plots have a good linear relationship. This phenomenon indicates that the adsorption of iodide species is almost no effect by the redox reaction on the (P-A) Gr/$NiCo_2O_4$ electrode surface.[34,35]

Table 2 EIS parameters of various CEs made from the impedance spectra.

Electrodes	R_s ($\Omega \cdot cm^{-2}$)	R_{ct} ($\Omega \cdot cm^{-2}$)	Z_w ($\Omega \cdot cm^{-2}$)	J_0 ($mA \cdot cm^{-2}$)	$\lvert I_{pc} \rvert$ ($mA \cdot cm^{-2}$)
Pt	7.55±0.02	3.63±0.02	0.63±0.02	1.24	3.16
Gr*	8.76±0.02	4.61±0.02	0.51±0.02	1.07	2.58
$NiCo_2O_4$*	9.98±0.02	6.78±0.02	1.39±0.02	0.91	2.52
(P-A) Gr/$NiCo_2O_4$	6.82±0.02	3.04±0.02	1.41±0.02	1.32	3.41

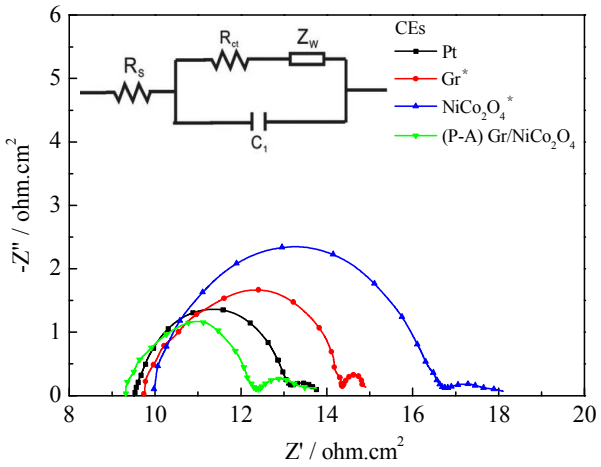

Fig. 8 Nyquist plots of the symmetrical Pt, Gr*, $NiCo_2O_4$* and (P-A) Gr/$NiCo_2O_4$ CEs for I^-/I_3^- redox couple.

Electrochemical impedance properties of different CEs are measured by using their symmetric cells. Fig. 8 exhibits the Nyquist plots of the symmetrical Pt, Gr*, $NiCo_2O_4$* and (P-A) Gr/$NiCo_2O_4$ CEs for I^-/I_3^- electrolyte and the corresponding EIS parameters are also listed in Table 2. The inset in Fig. 8 shows the equivalent circuit, in which the R_s is the resistance value at the onset point of the first semicircle, the R_{ct} is the radius of the first semicircle, and the semicircle at low frequency represents the Nernst diffusion impedance (Z_w) corresponding to the diffusion resistance of the I^-/I_3^- redox species.[36] As far as we know, R_s and R_{ct}, two crucial parameters for comparing the electrocatalytic ability of different CEs, are inversely correlated with the catalytic ability of electrodes. It can be seen from Table 2,

the R_s associated with the Pt, Gr*, $NiCo_2O_4$* and (P-A) Gr/$NiCo_2O_4$ CEs are 7.55±0.02, 8.76±0.02, 9.98±0.02, 6.82±0.02 Ω·cm^2, respectively. It is noted that the R_s of the Pt CE is comparable to that of the Gr* and $NiCo_2O_4$* CEs, but higher than that of (P-A) Gr/$NiCo_2O_4$ CE. The lower R_s for the (P-A) Gr/$NiCo_2O_4$ CE means a better electrical conductivity and more contact surface area than the other CEs. On the other hand, the CE with the smaller R_{ct} means the less overpotential for an electron transferring from the CE to the electrolyte, a facile electron transfer, and great electrochemical ability. From the Table 2, the R_{ct} for the Pt, Gr*, $NiCo_2O_4$* and (P-A) Gr/$NiCo_2O_4$ CEs are 3.63±0.02, 4.61±0.02, 6.78±0.02, 3.04±0.02 Ω·cm^2, respectively. The Pt CE has better electrochemical ability than the Gr* and $NiCo_2O_4$* CEs, however, with the graphene and PEDOT:PSS introduction, a smaller R_{ct} than that of the Pt CE produced from the (P-A) Gr/$NiCo_2O_4$ CE. Therefore, the graphene and PEDOT:PSS combinations are able to compete with the Pt CE for the DSSCs. Additionally, it should be noted that the Z_w for the (P-A) Gr/$NiCo_2O_4$ CE (1.41±0.02 Ω·cm^2) is a little larger than that of Pt electrode (1.39±0.02 Ω·cm^2). This can be attributed to the conductive polymers relatively low electrical conductivity compared with that of the Pt catalyst.

In addition to the EIS made from different materials, the influence of solvents on the electrochemical performance was also studied, and the key parameters of EIS are given in Table 1. As seen as Table 1, the values of R_s and R_{ct} for the CEs both follow the orders of (W-A) Gr/$NiCo_2O_4$ CE > (E-A) Gr/$NiCo_2O_4$ CE > (N-A) Gr/$NiCo_2O_4$ CE > (P-A) Gr/$NiCo_2O_4$ CE. These results are well agreement with the CVs, and ascribes to the same reasons.

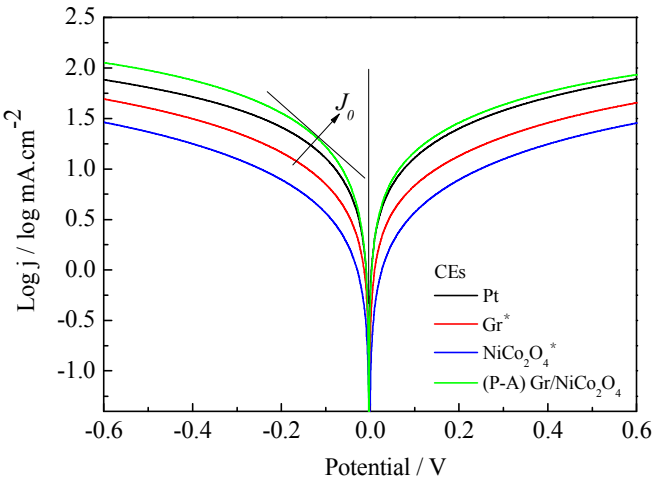

Fig. 9 Tafel curves of the symmetrical Pt, Gr*, $NiCo_2O_4$* and (P-A) Gr/$NiCo_2O_4$ CEs.

To further investigate the catalytic activities of the samples, Tafel polarization curves were obtained for the electrodes with Pt, Gr*, $NiCo_2O_4$* and (P-A) Gr/$NiCo_2O_4$ CEs in a dummy cell similar to the ones used in EIS

measurement as displayed in Fig. 9. Theoretically, the curve at low potentials (|U| < 0.12 V) represents the polarization zone, the one at the middle potentials (with a sharp slope) represents the Tafel zone, and the other at the high potentials (horizontal part) represents the diffusion zone. In Tafel polarization curve, usually presents logarithmic current density as a function of potential, and thus the corresponding exchange current density (J_0) for each CE can be evaluated from the extrapolated intercepts of the anodic and cathodic branches of the corresponding Tafel curves at the exchange current density axes also are summarized in Table 2. The J_0 for the (P-A) Gr/$NiCo_2O_4$ electrode is higher comparable to that of the Pt, Gr* and $NiCo_2O_4$* CEs; this means that the (P-A) Gr/$NiCo_2O_4$ electrode can trigger the reduction of I_3^- to I^- more effectively than the electrodes above mentioned. The R_{ct} can also be calculated by Eqn. (4) according to the relationship between J_0 and R_{ct} for the reduction of I_3^- ions to I^- ions.[37] According to the J_0 values and Eqn. (4), it can be deduced that the orders of the R_{ct} are $NiCo_2O_4$* CE > Gr* CE > Pt CE > (P-A) Gr/$NiCo_2O_4$ CE, which is great consistence with the CVs and EIS results. This indicates that (P-A) Gr/$NiCo_2O_4$ CE can be further explored to replace the expensive Pt as the catalyst for the Pt-free CE in DSSC, and in view of the fact that it is much cheaper than DSSC Pt-based and exhibits as high as power conversion efficiency. Furthermore, the influence of solvents to the performance of Tafel polarization curve was also investigated and the J_0 for the above mentioned CEs follow the same orders as the $|I_{pc}|$ (see Table 1).

3.5 Photovoltaic performance of DSSCs with different counter electrodes

Table 3 The influences of different CEs on the electrochemical performance and photoelectric properties of DSSCs.

Electrodes	V_{oc} *(V)*	J_{sc} *(mA·cm^{-2})*	*FF*	*PCEs (%)*	R_{ct1} *(Ω·cm^{-2})*	R_{ct2} *(Ω·cm^{-2})*
Pt	0.73	15.23	0.67	7.45	8.37±0.02	13.78±0.02
Gr*	0.71	13.49	0.60	5.75	9.91±0.02	22.77±0.02
$NiCo_2O_4$*	0.72	12.44	0.64	5.73	16.08±0.02	20.36±0.02
(P-A) Gr/$NiCo_2O_4$	0.75	16.12	0.67	8.10	6.83±0.02	10.94±0.02

J–V characteristics of the DSSCs with different CEs were measured under the optimization condition at 100 mW·cm^{-2} (AM 1.5 G) irradiation and are presented in Fig 10a. The corresponding parameters are listed in Table 3. The DSSC with a Pt CE shows the J_{sc} of 15.23 mA·cm^{-2}, V_{oc} of 0.73 V, *FF* of 0.67 and *PCE* of 7.43%, respectively. The DSSCs based on the Gr* and $NiCo_2O_4$* CEs exhibit the poor *PCEs* of 5.75% and 5.73% due to their poor electrocatalytic activity, and the detailed photovoltaic performance parameters are described in Table 3. When added

the graphene and PEDOT:PSS as the assistant of conductivity and catalyst, the DSSC with the (P-A) Gr/$NiCo_2O_4$ CE shows better J_{sc} of 16.12 mA·cm^{-2}, V_{oc} of 0.75 V, *FF* of 0.67 and *PCE* of 8.10%, respectively. Comparing the SEM image of $NiCo_2O_4$ particles, it may be said that the unique nanostructure of Gr/$NiCo_2O_4$ nanoparticles has larger effective surface area, which could led to the higher J_{sc} in favor of the DSSC (P-A) Gr/$NiCo_2O_4$-based. With the PEDOT:PSS assisted, the electrocatalytic activity is further enhanced, thus the device logically shows a better photovoltaic performance for the synergistic effect of graphene and PEDOT:PSS. Besides, the optimized (P-A) Gr/$NiCo_2O_4$-based DSSC shows a higher V_{oc} than the DSSCs with the others, which can be evidenced by the dark current characterization in Figure 10a. The (P-A) Gr/$NiCo_2O_4$-based DSSC possesses a smaller dark current at the same potential, suggesting a lower electron recombination rate for the optimized (P-A) Gr/$NiCo_2O_4$-based DSSC than the other DSSCs. Fig 10b shows the EIS of the DSSCs based on the Pt, Gr*, $NiCo_2O_4{}^*$ and (P-A) Gr/$NiCo_2O_4$ CEs and the corresponding parameters are listed in Table 3, in which the R_{ct1} means the interfacial charge-transfer resistance at the CE and electrolyte, and the R_{ct2} represents the interfacial charge-transfer resistance at the dye-sensitized photoanode and the electrolyte. From Fig 10b and Table 3, the (P-A) Gr/$NiCo_2O_4$-based DSSC exhibits a smaller R_{ct1} and R_{ct2} than the DSSCs with the Pt, Gr*, and $NiCo_2O_4{}^*$ CEs. This indicates that the (P-A) Gr/$NiCo_2O_4$ CE facilitates fast electron transport at the interface between I^-/I_3^- electrolyte and the electrodes, and it also can be deduced that the (P-A) Gr/$NiCo_2O_4$-based DSSC can indeed improve the charge recombination and has a more outstanding effect than in the other DSSCs.

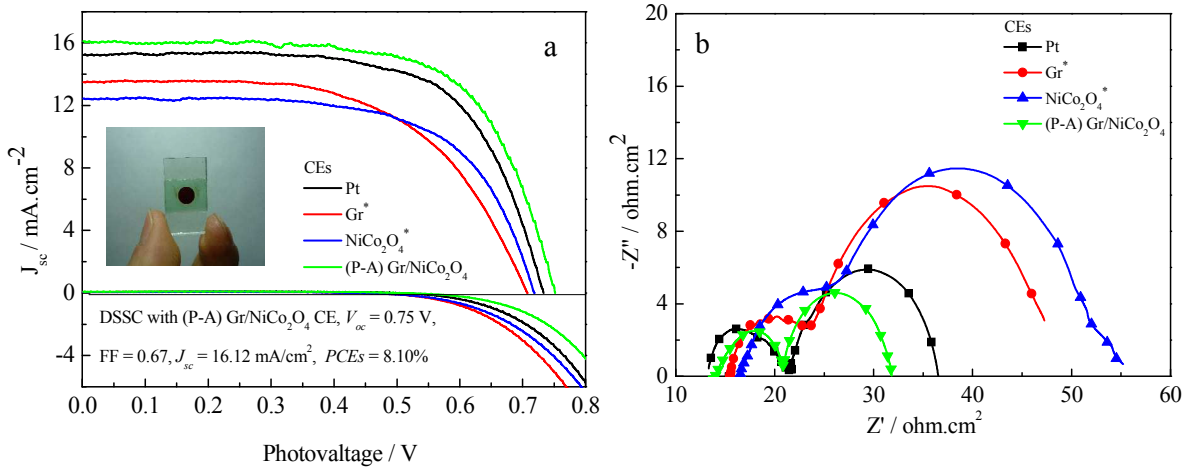

Fig. 10 *J-V* characteristics (a) and EIS spectra (b) of DSSCs fabricated with the Pt, Gr*, $NiCo_2O_4{}^*$ and (P-A) Gr/$NiCo_2O_4$ CEs under the standard illumination.

4. Conclusions

An efficient Gr/$NiCo_2O_4$ counter electrode with PEDOT:PSS assisted preparation as Pt-free CE and served in DSSC. Extensive electrochemical property study indicates that the (P-A) Gr/$NiCo_2O_4$ CE exhibits amazing electrocatalytic ability and low charge transfer resistance for the reduction of I_3^-, which can compares with that of Pt CE. Comparative studies found that the dye-sensitized TiO_2 nanorods show stronger absorbing capacity for the Uv-visible light and greater loading capability to the dye. The (P-A) Gr/$NiCo_2O_4$-based DSSC produces a remarkable improvement in short-circuit photocurrent, open circuit voltage and power conversion efficiency. Under the optimization conditions, the DSSC based on the (P-A) Gr/$NiCo_2O_4$ CE achieved an enhanced power conversion efficiency of 8.10% under irradiation of 100 $mW \cdot cm^{-2}$, comparable to that of the Pt-based DSSC (7.76%). The research presented here is far from being optimized but these profound advantages along with low-cost synthesis and scalable materials promise the new CE to be a great potential and strong candidate in robust DSSCs.

Acknowledgements

The authors are very grateful to the joint support by the National Natural Science Foundation of China (No. U1504624). This work is also supported by China Postdoctoral Science Foundation Funded Project (No. 2015M572102) and the Scientific Research Found of Henan Provincial Department of Science and Technology (No. 122300410107).

References

1 B. O'Regan and M. Grätzel, *Nature*, 1991, **353**, 737–740.

2 A. Yella, H. W. Lee, H. N. Tsao, C. Yi, A. K. Chandiran, M. K. Nazeeruddin, E. W. Diau, C. Y. Yeh, S. M. Zakeeruddin and M Grätzel, *Science*, 2011, **334**, 629–634.

3 S. Mathew, A. Yella, P. Gao, R. Humphry-Baker, B. F. E. Curchod, N. Ashari-Astani, I. Tavernelli, U. Rothlisberger, M. K. Nazeeruddin and M. Grätzel, *Nat. Chem*., 2014, **6**, 242–247.

4 M. Grätzel, *Nature*, 2001, **414**, 338–344.

5 F. Bella, C. Gerbaldi, C. Barolo and M. Grätzel, *Chem. Soc. Rev*., 2015, **44**, 3431–3473.

6 H. Choi, H. Kim, S. Hwang, Y. Han and M. Jeon, *J. Mater. Chem*., 2011, **21**, 7548–7551.

7 L. Kavan, J.-H. Yum and M. Grätzel, *Nano Lett*., 2011, **11**, 5501–5506.

8 H. Sun, Y. Luo, Y. Zhang, D. Li, Z. Yu, K. Li and Q. B. Meng, *J. Phys. Chem. C*, 2010, **114**, 11673–11679.

9 M. K. Wang, A. M. Anghel, B. Marsan, N. C. Ha, N. Pootrakulchote, S. M. Zakeeruddin and M. Grätzel, *J. Am. Chem. Soc*., 2009, **131**, 15976–15977.

10 M. X. Wu, Y. D. Wang, X. Lin, N. Yu, L. Wang, L. Wang, A. Hagfeldt and T. L. Ma, *Phys. Chem. Chem. Phys*., 2011, **13**, 19298–19301.

11 L. Kavan, J. H. Yum and M. Grätzel, *ACS Nano*, 2010, **5**, 165–172.

12 G. T. Yue, J. H. Wu, Y. M. Xiao, M. L. Huang, J. M. Lin, L. Q. Fan and Z. Lan, *Electrochim. Acta*, 2013, **92**, 64–70.

13 J.-Y. Lin, C.-Y. Chan and S.-W. Chou, *Chem. Commun*., 2013, **49**, 1440–1442.

14 G. Veerappan, K. Bojan and S.-W. Rhee, *ACS Appl. Mater. Interfaces*, 2011, **3**, 857–862.

15 C. Yuan, J. Li, L. Hou, X. Zhang, L. Shen and X. W. Lou, *Adv. Funct. Mater*., 2012, **22**, 4592–4597.

16 X. Y. Liu, Y. Q. Zhang, X. H. Xia, S. J. Shi, Y. Lu, X. L. Wang, C. D. Gu and J. P. Tu, *J. Power Sources*, 2013, **239**, 157–163**.**

17 B. Hua, W. Zhang, J. Wu, J. Pu, B. Chi and L. Jian, *J. Power Sources*, 2010, **195**, 7375–7379.

18 J. Li, S. Xiong, Y. Liu, Z. Ju and Y. Qian, *ACS Appl. Mater. Interfaces*, 2013, **5**, 981–988.

19 Y. Q. Wu, X. Y. Chen, P. T. Ji and Q. Q. Zhou, *Electrochim. Acta*, 2011, **56**, 7517–7522.

20 B. Sun, J. Zhang, P. Munroe, H.-J. Ahn and G. Wang, *Electrochem. Commun*., 2013, **31**, 88–91.

21 J. R. Mayhew, D. J. Bozym, C. Punckt and I. A. Aksay, *ACS Nano*, 2010, **4**, 6203–6211.

22 A. Debart, A. J. Paterson, J. Bao and P. G. Bruce, *Angew. Chem. Int. Ed*., 2008, **47**, 4521–4524.

23 L. L. Zhang, X. B. Zhang, Z. L. Wang, J. J. Xu, D. Xu and L. M. Wang, *Chem. Commun*., 2012, **48**, 7598–7600.

24 W. Q. Wu, B. X. Lei, H. S. Rao, Y. F. Xu, Yu-Fen Wang, C. Y. Su and D. B. Kuang, *Sci. Rep.*, 2013, **3**, 1–7.

25 G. T. Yue, J. H. Wu, Y . M. Xiao, J. M. Lin, M. L. Huang, Z. Lan and L. Q. Fan, *Electrochim. Acta*, 2012, **85**, 182–186.

26 Z. Lan, J. H. Wu, J. M. Lin and M. L. Huang, *J. Mater. Chem*., 2011, **21**, 15552–15557.

27 G. T. Yue, F. R. Tan, F. M. Li, C. Chen, W. F. Zhang, J. H. Wu and Q. H. Li, *Electrochim. Acta*, 2014, **149**, 117–125.

28 G. T. Yue, J. H. Wu, Y . M. Xiao, M. L. Huang, J. M. Lin and J.-Y. Lin, *J. Mater. Chem. A*, 2013, **1**, 1495–1501.

29 J. Y. Lin, W. Y. Wang and S. W. Chou, *J. Power Sources*, 2015, **282**, 348–357.

30 A. Hauch and A. Georg, *Electrochim. Acta*, 2001, **46**, 3457–3466.

31 Z.-Q. Li, Y.-P. Que, L.-E. Mo, W.-C. Chen, Y. Ding, Y.-M. Ma, L. Jiang, L-H. Hu and S-Y. Dai, *ACS Appl. Mater. Interfaces*, 2015, **7**, 10928–10934.

32 G. T. Yue, W. F. Zhang, J. H. Wu and Q. W. Jiang, *Electrochim. Acta*, 2013, **112**, 655–662.

33 W. J. Ke, G. J. Fang, H. Tao, P. L. Qin, J. Wang, H. W. Lei, Q. Liu and X. Z. Zhao, *ACS Appl. Mater. Interfaces*, 2014, **6**, 5525−5530.

34 S. Biallozor, A. Kupniewska, *Electrochem. Commun*., 2000, **2**, 480–486.

35 Y. Saito, W. Kubo, T. Kitamura, Y. Wada and S. Yanagida, *J. Photochem. Photobiol. A*, 2004, **164**, 153–157.

36 H.-M. Chuang, C.-T. Li, M.-H. Yeh, C.-P. Lee, R. Vittal and K.-C. Ho, *J. Mater. Chem. A*, 2014, **2**, 5816–5824

37 G. T. Yue, J. H. Wu, J.-Y. Lin, Y . M. Xiao, J. M. Lin, M. L. Huang and Z. Lan, *Carbon*, 2013, **55**, 1–9.

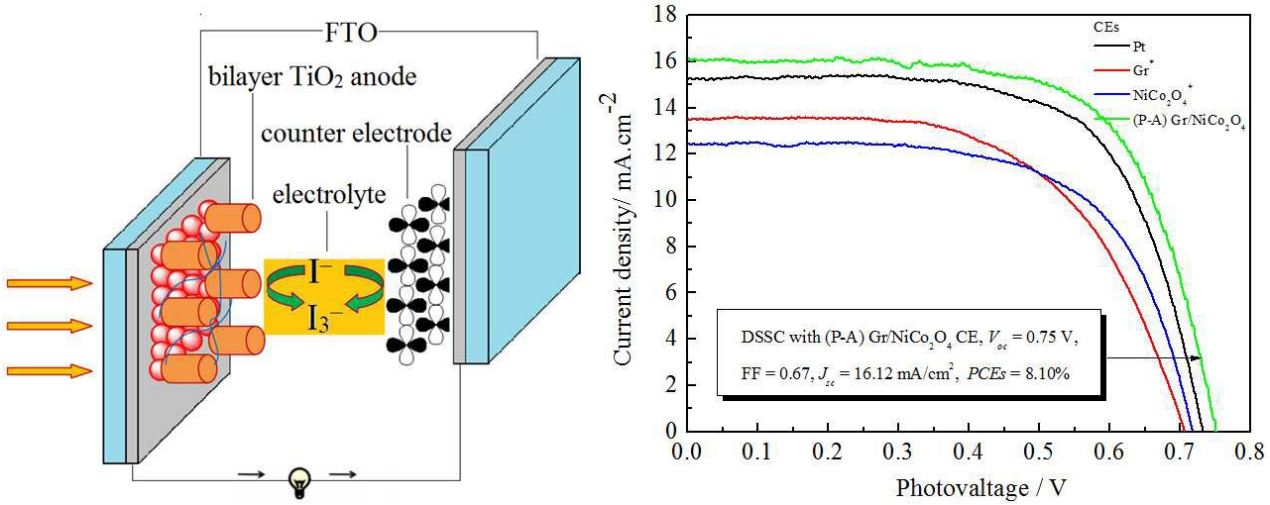

Much higher photovoltaic performance of dye-sensitized solar cell with (P-A) Gr/$NiCo_2O_4$ counter electrode as well as that of Pt configuration device.